Chemical Engineering Journal 410 (2021) 128340

Contents lists available at ScienceDirect

Chemical Engineering Journal

journal homepage: www.elsevier.com/locate/cej

A high-performance oxygen evolution electrode of nanoporous Ni-based solid solution by simulating natural meteorites

Boya Hao [a], Zhiguo Ye [a,*], Jilin Xu [a,*], Liangliang Li [a], Juntong Huang [a], Xinyuan Peng [a], Duosheng Li [a], Zhong Jin [b,*], Guang Ma [c]

[a] School of Materials Science and Engineering, Nanchang Hangkong University, Nanchang 330063, China
[b] Key Laboratory of Mesoscopic Chemistry of MOE, Jiangsu Key Laboratory of Advanced Organic Materials, School of Chemistry and Chemical Engineering, Nanjing University, Nanjing, Jiangsu 210023, China
[c] Global Energy Interconnection Research Institute Co., Ltd, Beijing 102209, China

ARTICLE INFO

Keywords:
Gibeon meteorites
Nanoscale Kirkendall effect
Nanoporous solid solution
Oxygen evolution reaction
Electrochemical stability

ABSTRACT

Transforming the intermittent solar and wind energies into green hydrogen energy by water electrolysis is deemed to be a promising approach to substitute traditional fossil energies. However, the scarcity of precious IrO_2/RuO_2-based metal oxides for oxygen evolution reaction hinders the large-scale utilization. Here, based on the nanoscale Kirkendall effect, we fabricate nanoporous γ-Ni based solid solution with the simulated FeCoNi surface compositions of Gibeon meteorites by a facile microwave sintering method. A metal (oxy)hydroxide layer with a thickness of approximately 9 nm was formed on the surface of as-prepared electrode after aging, achieving an overpotential of only 254 mV at 10 mA cm^{-2} and a low Tafel slope of 37.0 mV dec^{-1}. The electrode exhibits outstanding long-term stability in a wide range of current densities without compromising the electrocatalytic activity, which is attributed to the 3D-interconnected nanoporous structure, synergistic effect of different species, high conductivity and excellent wettability. The fabrication of nanoporous non-precious solid solution architectures which mimic naturally-formed materials provides a feasible strategy for the design of high-performance electrocatalysts towards clean energy applications.

1. Introduction

The rising consumption of fossil fuels (coal and petroleum) is causing the deterioration and pollution of air and water, seriously threatening the living environment of human being. In recent years, the exploitation of clean and sustainable energy sources has aroused more and more attention [1–3]. Renewable hydrogen (H_2) energy derived from the conversion of intermittent wind and solar power via electrochemical water splitting is considered as one of the promising substitutions of traditional fossil energies. However, the sluggish kinetics of the oxygen evolution reaction (OER) is one the main reasons of the relatively low electrolytic efficiency for water splitting. Precious metal oxides (i.e. IrO_2 and RuO_2) coated on titanium substrates have the merits of low resistivity ($3 \sim 6 \times 10^{-5}$ Ω cm), excellent electrocatalytic activity, long service life and decent mechanical strength for the OER in acid medium, but the high costs and scarcity impede their wide application [4–8]. For realizing the large-scale application of electrochemical water splitting, the OER electrode should possesses the characteristics of high electrocatalytic activity, superior stability, good wettability, low cost and environment friendliness.

To obtain affordable electrode materials, the compounds of VIII 3d metals (such as Fe, Co, and Ni) with various forms (i.e., oxides, sulfides, selenides, phosphides and borides etc.) had been widely explored for the OER, because of the abundant sources and the same outermost electron configurations with Ru, Ir and Pt [9–21]. In alkaline mediums, many Fe-, Co-, and Ni-based nanostructural OER electrocatalysts exhibit the electrocatalytic activity even higher than RuO_2- and IrO_2- based oxides [9–31]. At present, the major problem of these nanostructured electrocatalysts towards large-scale application is to achieve long working life without compromising their electrocatalytic activity [1]. In particular, the OER process usually requires high current densities (>500 mA cm^{-2}) in practice [3], which may easily makes the nanostructural electrodes (i.e., nanowires, nanosheets, etc.) inactive owing to the accumulation and impact of oxygen bubbles. Formal et al. reported that a Gibeon meteorite with the surface compositions of Fe-Co-Ni ($Fe_{0.34}Co_{0.11}Ni_{0.55}$) could deliver low overpotential of 270 mV (at 10 mA cm^{-2}), small Tafel slope

* Corresponding authors.
E-mail addresses: yezhiguo2008@163.com, 70125@nchu.edu.cn (Z. Ye), jlxu@nchu.edu.cn (J. Xu), zhongjin@nju.edu.cn (Z. Jin).

https://doi.org/10.1016/j.cej.2020.128340
Received 27 October 2020; Received in revised form 21 December 2020; Accepted 27 December 2020
Available online 2 January 2021

of 37 mV decade^{-1} and superior stability of >1000 h (at 500 mA cm^{-2}) for the OER in alkaline solution [32]. The Gibeon meteorite also exhibited a reconstruction of surface compositions and structure during the OER process, further improving the electrocatalytic activity [33]. However, the scarcity of Gibeon meteorites limits the large-scale application as OER electrocatalyst for clean H_2 production.

Inspired by the above analysis, we propose the fabrication of artificial alloy materials with simulated surface compositions of Gibeon meteorites for electrocatalytic water splitting. Furthermore, it is reasonable that the construction of nanostructured porous materials with ultra-large specific surface area can further raise the catalytic activity towards OER. In this work, we use a microwave-sintering approach to fabricate nanoporous FeCoNi solid solution electrodes with nanoscale Kirkendall porosity and the metal atom composition similar to Gibeon meteorites after aging. The Mg powder is employed as the pore-making agent. The nanoscale Kirkendall porosity (see Fig. 1a) was formed due to the different diffusion coefficients of the vacancies/atoms between different materials, which has been previously utilized to synthesize hollow nanocrystals with diverse sizes and morphologies [33–40]. Moreover, compared to the conventional thermal heating method, the microwave-sintering method has the intrinsic advantages of enhanced diffusion processes, increased internal vacancies, low sintering temperatures and improved mechanical properties, etc. [41,42] The as-prepared nanoporous Ni-based solid solution electrodes exhibit excellent electrocatalytic activity, superior stability, certain mechanical strength, good wettability, low cost and environment friendliness, making the large-scale application of electrocatalytic water splitting a real possibility.

2. Results and discussion

2.1. Synthesis and characterizations

Fig. 1a exhibits the fabrication procedure of nanoporous FeCoNi solid solution electrodes formed by the nanoscale Kirkendall effect during the process of microwave-sintering. The nanopores and nanoparticles are formed on account of the different inter-diffusion rates of atoms/vacancies on the solid/liquid and solid/solid interfaces, realizing the formation of nanoscale Kirkendall porosity. During the microwave-sintering process, the melted Mg acted as the pore-making agent to form lots of solid/liquid interfaces, which were favourable for raising atom/vacancy diffusion velocity, increasing the diffusion interface area, raising the rate of grain boundary migration and decreasing the sintering temperature at the interfaces [33]. Figure S1 shows that the sample without Mg (the No.1 sample in Table S1) cannot form nanoporous structure, confirming that the importance of Mg as the pore-making agent for the fabrication of nanoporosity [33–40]. Figure S2 show schematic diagram of the nanoscale Kirkendall effect in bulk phase diffusion couples (i.e. Ni–Fe, Ni–Co, Co–Fe, Ni–Mg, Co–Mg, Fe–Mg). The different diffusion rates of atoms/vacancies in bulk phase resulted in the unequal material flow and the aggregation of excess vacancies, which gave rise to the formation of interconnected nanopores and nanogaps in the regions with faster diffusing components. The microwave field also accelerates the diffusion rates of atoms/vacancies and the grain boundary migration, leading to the formation of nanopores and nanoparticles [41–43]. Meanwhile, microwave-sintering process can uniformly heat the interior and exterior parts of the sample, enabling the formation of homogeneous nanopores and nanoparticles. In addition, the short time of microwave-sintering (20 min) can advantageously avoid the formation of large pores owing to the merging of nanopores. These advantageous factors enable the formation of nanostructured solid solution alloy materials with Kirkendall nanopores and large specific surface area, favorably obtaining superior electrocatalytic activity and long-term stability for the OER.

The nominal composition of Fe, Co and Ni in as-prepared sample is designed to confirm to the metal atom compositions on the surface of the Gibeon meteorites [21]. The samples with other compositions also are fabricated for the control (Table S1). Clearly, the actual content of Fe, Co and Ni in bulk samples is basically consistent with the nominal composition and a small quantity of Mg has been diffused into the solid solution in addition to acting as the pore-making agent (Table S2 and Figure S3). Hence, the scanning electron microscopy (SEM) and high-resolution TEM (HRTEM) images displayed in Fig. 1b, d and e is the surface morphology of nanoporous FeCoNiMg solid solution (NP-FeCoNiMg-SS, corresponding to the No.8 sample in Table S1) prepared by microwave-sintering at 900 °C for 20 min (denoted as NP-FeCoNiMg-SS-900). NP-FeCoNiMg-SSs sintered at 700 °C, 800 °C, 1000 °C and 1100 °C denote as NP-FeCoNiMg-SS-700, NP-FeCoNiMg-SS-800, NP-FeCoNiMg-SS-1000 and NP-FeCoNiMg-SS-1100, respectively. After sintering, the precursor Ni, Fe and Co powders with the sizes of approximately 5–50

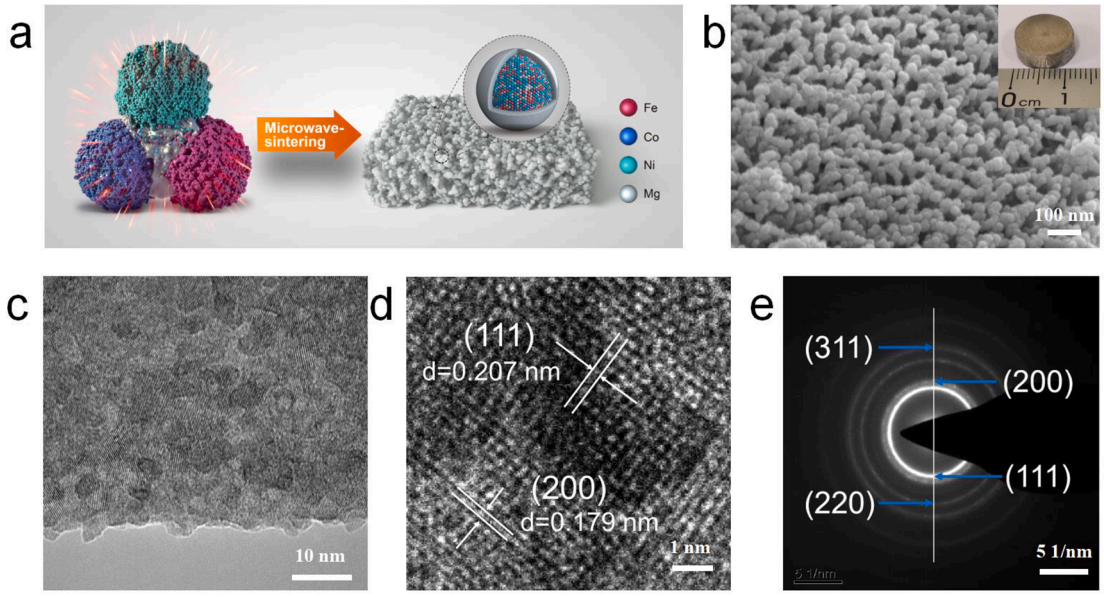

Fig. 1. Synthesis and structural characterizations of nanoporous FeCoNi solid solutions. (a) Schematic illustration of the preparation method of nanoporous FeCoNi solid solutions. (b) FESEM, (c) TEM, (d) HRTEM images and (e) SAED pattern of NP-FeCoNiMg-SS-900, respectively. The insert in (b) displays an optical photograph of NP-FeCoNiMg-SS-900.

μm (Figure S4) have been transformed into nanopores and interconnected nanoparticles with the diameters of 5–20 nm owing to the nanoscale Kirkendall effect, as shown in Fig. 1b. The transmission electron microscopy (TEM) image in Fig. 1c further exhibits the morphology of NP-FeCoNiMg-SS-900 with high contrast originated from the random distribution of alloy nanoparticles. The HRTEM image and corresponding selective area electron diffraction (SAED) pattern of NP-FeCoNiMg-SS-900 (Fig. 1d, e) exhibit multi-crystalline lattice fringes and diffraction rings, which can be indexed to the (111), (200), (220) and (311) planes of γ-Ni based solid solution [44]. With a lower sintering temperature of 800 °C, the sample of NiFeCoMg-SS-800 exhibits a 3D structure consisting of ultrathin nanosheets with the thickness of several nanometers (Figure S5a, b). With the sintering temperatures of 1000 °C and 1100 °C, the samples of NiFeCoMg-SS-1000 and NiFeCoMg-SS-1100 show obvious aggregation owing to the higher sintering temperatures (Figure S5c-f), indicating that the sintering temperature has great influence on the surface morphology of products. Compared to the samples sintered at 900 °C, 1000 °C and 1100 °C, NiFeCoMg-SS-800 possesses lower number of vacancies and lower diffusion rates of atoms/vacancies, which is easier to form two-dimensional ultrathin nanosheets. With an increase of sintering temperature, the number of vacancies and the diffusion rates of atoms/vacancies rapidly increase, easily leading to a formation of nanoparticles and obvious aggregation.

The crystalline structures and surface compositions of the samples were further evaluated by X-ray diffraction (XRD) and X-ray photoelectron spectroscopy (XPS), as shown in Fig. 2. As a control sample, pristine nanoporous Ni (NP-Ni) was also prepared with the similar procedure of NP-FeCoNiMg-SS-900, as shown in Figure S6. Fig. 2a exhibits the XRD patterns of NP-FeCoNiMg-SS and NP-Ni electrodes prepared at different sintering temperatures. The NP-FeCoNiMg-SS samples prepared at 800–1100 °C show three diffraction peaks located around 43.8°, 50.0° and 75.0°, corresponding to the (111), (200) and (220)

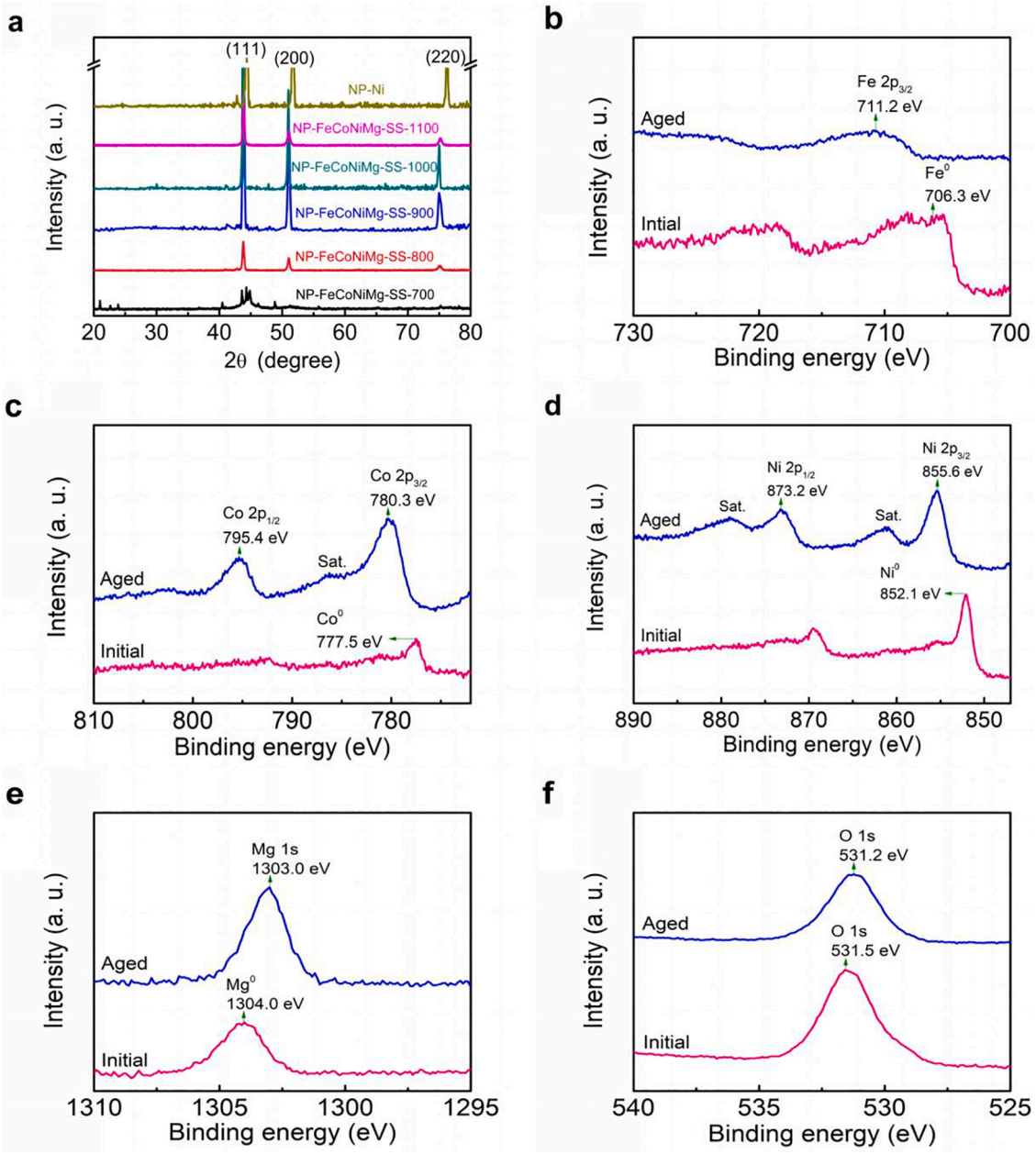

Fig. 2. Crystalline phase and surface composition characterizations. (a) XRD patterns of NP-FeCoNiMg-SS and NP-Ni electrodes sintered at different temperatures. (b-e) High-resolution XPS spectra at (b) Fe 2p, (c) Co 2p, (d) Ni 2p, (e) Mg 1s and (f) O 1s regions of NP-FeCoNiMg-SS-900 electrode before and after long-term OER test in 1 M KOH solution at 1000 mA cm^{-2} for 1000 h.

planes of γ-Ni solid solution with a face-centered cubic (FCC) structure [44]. Meanwhile, compared to the NP-Ni sample, the diffraction peaks of NP-FeCoNiMg-SS samples exhibit obvious deviations, owing to the incorporation of Fe, Co and Mg elements in the alloys. With the sintering temperature of 700 °C, the diffraction peaks of NP-FeCoNiMg-SS-700 are different from the other NP-FeCoNiMg-SS samples obtained at higher temperatures, indicating that the phase of γ-Ni solid solution has not been formed in NP-FeCoNiMg-SS-700 due to the low sintering temperature. Figure S7 displays the XRD results of the samples with different compositions. The decrease of Ni content in the sample obviously resulted in the formation of α-Fe solid solution and a little $CoMg_2$ phase.

The outermost active species anchored on the surface of electrocatalysts are the crucial factors to determine the electrocatalytic activity for the OER [45]. In the XPS spectra of pristine NP-FeCoNiMg-SS-900, the peaks located at 706.3 eV (Fig. 2b), 777.5 eV (Fig. 2c), 852.1 eV (Fig. 2d) and 1304.0 eV (Fig. 2e) are corresponding to the energy levels of Fe^0, Co^0, Ni^0 and Mg^0, respectively. During long-term OER processes, a metal (oxy)hydroxide layer will be formed on the surface of NP-FeCoNiMg-SS electrodes, leading to superior electrocatalytic activity and ultra-long working life. To identify the surface compositions after aging, XPS analysis was performed on the NP-FeCoNiMg-SS-900 electrode after the OER operation for 1000 h at 1000 mA cm^{-2} in 1 M KOH solution (Fig. 2b-f), revealing the presence of Fe, Co, Ni, Mg and O elements. A broad bump located at 711.2 eV in the Fe 2p spectrum of the aged NP-FeCoNiMg-SS-900 (Fig. 2b) corresponds to the Fe $2p_{3/2}$ signals of Fe^{2+} or Fe^{3+}, which should be attributed to the very low concentration of Fe (~4%) in the outer (oxy)hydroxide phase and the similar binding energies of Fe^{2+} and Fe^{3+} species (710 eV *vs.* 711 eV) [32,46–48]. The Co 2p spectrum of the aged electrode (Fig. 2c) displays two major peaks at 795.4 eV (Co $2p_{1/2}$) and 780.3 eV (Co $2p_{3/2}$), respectively, consistent with the binding-energy separation of CoOOH or Co_2O_3 phase [32,49]. The Ni 2p spectrum of the aged electrode in Fig. 2d exhibits a doublet at 873.2 eV and 855.6 eV, respectively, corresponding to the Ni $2p_{1/2}$ and Ni $2p_{3/2}$ signals of Ni^{2+}, which is in accord with the $Ni(OH)_2$ phase [32,50]. Fig. 2e shows the Mg 1s spectrum of the aged electrode with an obvious peak located at 1303.0 eV, corresponding to the $Mg(OH)_2$ phase [51]. Moreover, an obvious shift of the oxygen peak on the pristine and aged electrode is observed from 531.5 eV to 531.2 eV (Fig. 2f). The O1s spectra before and after aging can be decomposed into four characteristic peaks of O1-530.2 eV for metal–oxygen bounds, O2-531.2 eV for defective oxygen of low coordination, O3-532.1 eV for hydroxyl groups and O4-533.3 eV for adsorbed water (Figure S8) [8,22]. These indicate that all the Fe, Co, Ni and Mg species are in the (oxy) hydroxide forms, confirming the formation of a metal (oxy)hydroxide layer on the surface of NP-FeCoNiMg-SS-900 electrode after long-term OER operation. The XPS analysis results reveal that the metal (oxy)hydroxide layer formed on the surface of aged NP-FeCoNiMg-SS-900 electrode has a metal cation stoichiometry of $Fe_{0.04}Co_{0.22}Ni_{0.34}Mg_{0.40}$ (Table S4). In contrast, the pristine NP-FeCoNiMg-SS-900 electrode possesses an ultrathin metal oxide layer with the surface compositions of $Fe_{0.23}Co_{0.09}Ni_{0.56}Mg_{0.12}$ (Table S4), which is clearly different with the metal (oxy)hydroxide layer formed after long-term OER operation in alkaline medium. Figure S9 further displays atomic composition profile obtained from XPS of pristine and aged NP-FeCoNiMg-SS-900 at a current density of 10 mA cm^{-2} in 1 M KOH electrolyte. Clearly, the O atomic composition on the outermost surface of pristine and aged NP-FeCoNiMg-SS-900 is far higher than that of the inner bulk. With the increase of etching depth from zero to 20 nm, the O atomic composition rapidly decrease and the Fe, Co and Ni quickly increase, indicating an ultrathin metal (oxy)hydroxide layer on the surface of pristine and aged NP-FeCoNiMg-SS-900.

The mechanical performance of the electrodes usually needs to be considered in modern industries such as chlorine alkali industry, electroplating, electrochemical wastewater treatment, electrochemical synthesis, electrochemical anodic oxidation, etc., which is one of the key performance indicators for practical applications owing to the harsh conditions during the electrochemical processes at large current densities. In most cases, metal substrates with excellent mechanical properties (such as pure titanium plates) are usually employed to fabricate the industrial electrode materials for large-scale electrocatalytic applications. To evaluate the mechanical properties of 3D-interconnected NP-FeCoNiMg-SS electrodes, the compressive stress–strain curves were measured (Fig. 3a), and the compressive strength and elastic modulus of the samples were calculated from the stress–strain curves, as exhibited in Fig. 3b. The compressive stress–strain curve of NP-FeCoNiMg-SS electrode sintered at 1100 °C show no fracture during the compression process owing to excellent ductility (Fig. 3a). As the sintering temperature increased from 800 °C to 1100 °C, the compressive strength of the electrodes increased from 101 MPa to 1388 MPa, which should be attributed to the decrease of porosity and the increase of density at high sintering temperatures (Figure S10). This result is also consistent with the morphology variations of the samples (Figure S3 and Figure S5). The elastic moduli of NP-FeCoNiMg-SS electrodes obtained at 800 °C, 900 °C, 1000 °C and 1100 °C are measured to be 0.86 GPa, 2.31 GPa, 2.96 GPa and 2.03 GPa, respectively (Fig. 3b). The compressive strength and elastic modulus of NP-FeCoNiMg-SS electrodes can satisfy the requirements of mechanical strength and flexibility for the applications in water-electrolysis units.

2.2. Electrocatalytic performances.

To compare the OER activity, the linear sweep voltammetry (LSV) curves of NP-FeCoNiMg-SS, NP-Ni, and IrO_2/Ti electrodes were

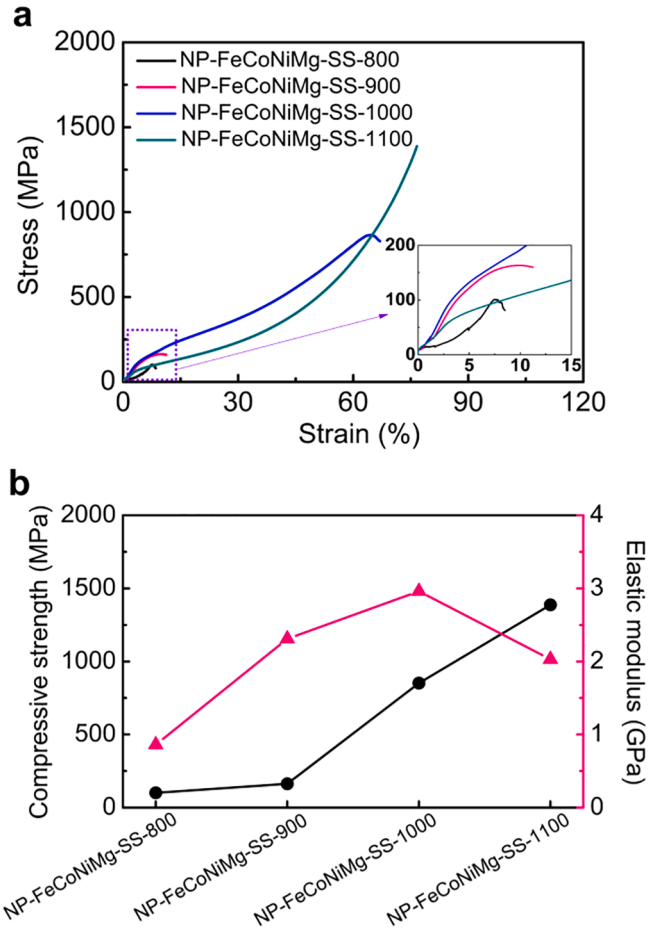

Fig. 3. Measurements of mechanical properties. (a) Typical compressive stress–strain curves and (b) Compressive strength and elastic modulus of NP-FeCoNiMg-SS electrodes obtained at different sintering temperatures.

measured in 1 M KOH solution at 1 mV s^{-1} without *iR*-compensation (Fig. 4a). Obvious current peaks between 1.35 and 1.45 V (*vs.* RHE) are shown in the LSV curves of NP-FeCoNiMg-SS and NP-Ni electrodes, corresponding to the oxidation of the metal species on the electrode surface into a metal (oxy)hydroxide layer [3,52,53]. Clearly, the oxidation peak of NP-FeCoNiMg-SS electrodes with different sintering temperatures locate at approximately +1.424 V (*vs.* RHE) overlaps with the onset of the OER, as shown in Fig. 4a. For NP-Ni electrode, the oxidation peak located at about +1.398 V (*vs.* RHE) occurs clearly prior to its OER onset. The different content of Fe, Co and Ni leads to an obvious change of the oxidation wave for as-prepared electrodes (see Figure S11). These peak feature of pre-OER oxidation hint the change of the active phases before and after OER as well as the distinction of the active phases owing to different atomic ratio of Fe, Co and Ni [54]. Compared to NP-Ni and IrO_2/Ti electrodes, the NP-FeCoNiMg-SS-900 electrode exhibits higher current densities on the same potential, indicating its superior electrocatalytic activity. In addition, the NP-FeCoNiMg-SS-900 electrode display the highest OER activity among all the as-prepared samples with different sintering temperature and composition (Fig. 4a and Figure S11). NP-FeCoNiMg-SS-900 electrode also is measured in 0.1 M KOH, 1 M KOH, 30 wt% KOH and 1 M Na_2SO_4 solutions (Figure S12), exhibiting a better electrocatalytic performance at a media of higher OH^- content. Fig. 4b shows the iR_s-corrected Tafel plots of these electrodes derived from the LSV curves in Fig. 4a. The Tafel slope of NP-FeCoNiMg-SS-900 electrode is 37.0 mV dec^{-1}, which is much smaller than those of NP-FeCoNiMg-SS-800 (51.6 mV dec^{-1}), NP-FeCoNiMg-SS-1000 (66.9 mV dec^{-1}), NP-FeCoNiMg-SS-1100 (71.7 mV dec^{-1}), NP-Ni (103.0 mV dec^{-1}) and IrO_2/Ti electrodes (62.7 mV dec^{-1}). Table S5 compares the Tafel slopes of NP-FeCoNiMg-SS-900 electrode with some recently advanced transition metal-based

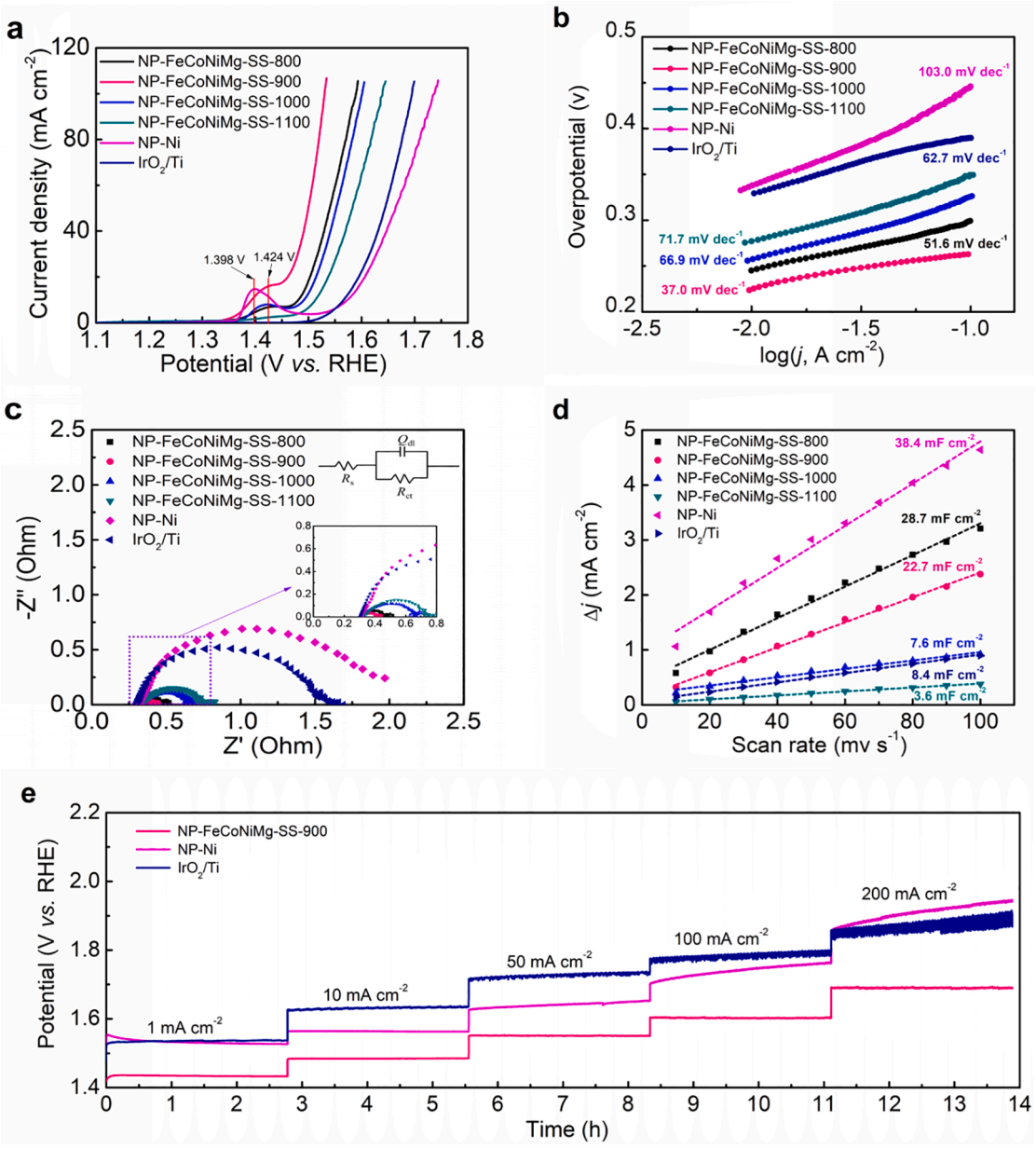

Fig. 4. Electrocatalytic measurements. (a) LSV curves of NP-FeCoNiMg-SS, NP-Ni, and IrO_2/Ti electrodes measured in 1 M KOH solution at a scan rate of 1 mV s^{-1} without iR_s-compensation. (b) The corresponding iR_s-corrected Tafel slopes of the electrodes calculated from the LSV curves in (a). (c) Nyquist plots of the electrodes measured at an OER voltage 1.567 V (*vs* RHE) over the frequency range 100000–0.01 Hz in 1 M KOH. The insets are the equivalent circuit of $R_s(Q_{dl}R_{ct})$ and the plots at high frequency region, respectively. (d) The C_{dl} values of NP-FeCoNiMg-SS, NP-Ni, and IrO_2/Ti electrodes measured in 1 M KOH solution. (e) Consecutive galvanostatic measurements of the electrodes measured in 1 M KOH solution at 1, 10, 50, 100, and 200 mA cm^{-2}, respectively.

electrocatalysts for OER, which obviously confirms the superiority of NP-FeCoNiMg-SS-900 electrode toward OER. To further insight into OER kinetics, the analysis of electrochemical impedance spectroscopy (EIS) was employed at an OER voltage 1.567 V (*vs* RHE) (Fig. 4c and the insets). The equivalent circuit, $R_s(Q_{dl}R_{ct})$, is employed to fit the EIS data of these samples for the OER. R_s represents the solution resistance, Q_{dl} corresponds to the double-layer capacitance and R_{ct} is the charge-transfer resistance during the OER process. The fitted data derived from the EIS of these samples are displayed in Table S6. As shown in the figure, a low charge transfer resistance (R_{ct}) of 0.097 Ω cm^{-2} is fitted for NP-FeCoNiMg-SS-900 electrode, which is much smaller than those of NP-FeCoNiMg-SS-800 (0.145 Ω cm^{-2}), NP-FeCoNiMg-SS-1000 (0.314 Ω cm^{-2}), NP-FeCoNiMg-SS-1100 (0.389 Ω cm^{-2}), NP-Ni (1.466 Ω cm^{-2}) and IrO_2/Ti electrodes (1.201 Ω cm^{-2}). It also is discovered that the fitted Q_{dl} values of NP-FeCoNiMg-SS, NP-Ni and IrO_2/Ti electrodes are basically consistent with double layer capacitance (C_{dl}) values in Fig. 4d. The Table S5 exhibits the electrocatalytic activities for some advanced electrocatalysts for OER. The Tafel slopes and R_{ct} of NP-FeCoNiMg-SS-900 electrode are lower than that of these electrodes, especially the R_{ct}, which should be attributed to nanoporous structure, high conductivity, and synergistic effect of Fe, Co and Ni species. NP-FeCoNiMg-SS-900 electrode also possesses an outstanding Faradaic efficiency of 97.6% in an alkaline medium (Figure S13).

The superior electrocatalytic activity of NP-FeCoNiMg-SS-900 electrode for the OER is attributed to its high electrochemically active surface area (ECSA), high conductivity and the synergistic effects of different species. The NP-FeCoNiMg-SS-900 electrode has high porosity and large specific surface area, providing the ultra-large ECSA for the OER. The 3D interconnected nanostructure of NP-FeCoNiMg-SS-900 electrode with an outermost shell of surface (oxy)hydroxide layer ensures high local and overall electrical conductivity for charge transfer. The NP-FeCoNiMg-SS-900 electrode also possesses excellent hydrophilicity and wettability owing to its developed hierarchical porous structure (video S1 and Figure S3). The synergistic effects mainly should be ascribed to two following aspects [52,54–60]. (1) The Co incorporation in NP-FeCoNiMg-SS-900 electrode can further improves the conductivity of surface (oxy)hydroxide layer derived from the synergy of multiple metal species, consequently facilitating the proton migration and electron transport over electrode and lowering the onset OER potential; (2) The Fe is essential for the metal (Ni and/or Co) (oxy)hydroxide layer to achieve high OER activity, which is attributed to the synergistic effect owing to the synergy with the adjacent Ni or Co sites through forming O-bridged Fe-metal reaction centers.

To further insight the intrinsic activity, specific activity, which is the current per unit real surface area of the electrocatalyst (i.e., mA $cm^{-2}_{electrocatalyst}$ at a given OER potential), mainly relies on the determination of the surface area [61]. The C_{dl} is currently the most popular method for measuring the ECSAs of metal oxides. A specific capacitance of 40 μF cm^{-2}_{oxide}, which is considered as a universal value for metal oxide surfaces, is employed to calculate the ECSAs by using the C_{dl} values. As exhibited in Fig. 4d and Figure S14, the NP-FeCoNiMg-SS-800, NP-FeCoNiMg-SS-900, NP-FeCoNiMg-SS-1000, NP-FeCoNiMg-SS-1100, NP-Ni and IrO_2/Ti electrodes achieve the C_{dl} values of 28.7 mF cm^{-2}, 22.7 mF cm^{-2}, 7.6 mF cm^{-2}, 3.6 mF cm^{-2}, 38.4 mF cm^{-2} and 8.4 mF cm^{-2}, respectively. The C_{dl} values divided by 40 μF cm^{-2}_{oxide} are the ECSAs, as shown in Table S7. Finally, the specific activity can be calculated by applying the current densities at a OER potential of 1.53 V (*vs.* RHE) in Fig. 4a. The specific activities of NP-FeCoNiMg-SS-800, NP-FeCoNiMg-SS-900, NP-FeCoNiMg-SS-1000, NP-FeCoNiMg-SS-1100, NP-Ni and IrO_2/Ti electrodes are 0.057 mA cm^{-2}, 0.175 mA cm^{-2}, 0.161 mA cm^{-2}, 0.183 mA cm^{-2}, 0.005 mA cm^{-2} and 0.014 mA cm^{-2}, respectively (Table S7). Obviously, the NP-FeCoNiMg-SSs possess far higher intrinsic activity than the NP-Ni, which should be attributed to the synergistic effects of Fe, Co and Ni species in the surface metal (oxy)hydroxide layer formed on the electrode surface after aging. The NP-FeCoNiMg-SS-900, NP-FeCoNiMg-SS-1000 and NP-FeCoNiMg-SS-1100 have similar intrinsic activity, but far higher than NP-FeCoNiMg-SS-800 electrodes, which should be the consequence of low sintering temperature that results in an insufficient alloying (see Fig. 2a).

It is known that the actual current densities for OER in the LSV curves are difficultly distinguished owing to the presence of oxidation peaks, especially at low current densities. To reveal the actual OER current densities, the multi-step consecutive chronopotentiometric curves of NP-FeCoNiMg-SS-900, NP-Ni, and IrO_2/Ti electrodes were performed (Fig. 4e). These electrodes were subjected to a long-term OER process of 50,000 s at different current densities ranged from 1 to 200 mA cm^{-2}. When the OER current density reaches 1 mA cm^{-2} at the potential, the NP-FeCoNiMg-SS-900, NP-Ni, and IrO_2/Ti electrodes show the overpotentials of 204, 301, and 306 mV, respectively. At the current density of 10 mA cm^{-2}, the overpotentials of the above-mentioned electrodes reach 254, 334, and 402 mV, respectively. Clearly, the overpotentials of NP-FeCoNiMg-SS-900 electrode at the same current densities are much lower than those of NP-Ni and IrO_2/Ti electrodes. These results indicate that the electrocatalytic activity of NP-FeCoNiMg-SS-900 electrode can compare favourably with other state-of-the-art OER electrocatalysts (Table S5).

The long-term stability of NP-FeCoNiMg-SS-900 electrode in alkaline medium was also compared with other representative electrodes in Fig. 4e. The OER potential of NP-FeCoNiMg-SS-900 electrode exhibits almost no fluctuation during the long-term electrolysis process for totally 50,000 s at different current densities, confirming its great operation stability. In contrast, the NP-Ni and IrO_2/Ti electrodes display obvious potential increases at the large current densities of 100 and 200 mA cm^{-2} as the time goes on, indicating their inferior stability in alkaline medium under large current densities. The reusability of NP-FeCoNiMg-SS-900 electrode was further evaluated by the consecutive OER polarization curves (Figure S15). After 1000 cycles of repeated potential scans between 1.0 and 1.5 V, the OER activity of NP-FeCoNiMg-SS-900 electrode exhibits a slight increase, indicating its good reusability. When working at a large current density of 1000 mA cm^{-2}, the bath potential of NP-FeCoNiMg-SS-900 electrode for the OER remains approximately 3.5 V over time (Figure S16), confirming its superior long-term stability without compromising the electrocatalytic activity under large current densities. Figure S17 exhibits the LSV curves of FeCoNiMg-SS-900 electrode after different aged times at the current density of 1000 mA cm^{-2}, further proving the catalytic performance will be slightly increased. With an increase of aged time, the redox peak of NP-FeCoNiMg-SS-900 electrode in the CV curves shifts to lower potential and the peak area increases (Figure S18), indicating a composition re-arrangement possibly derived from the decrease of the Fe content on the (oxy)hydroxide layer surface, which is consistent with the literature. [52,55] Table S4 showed a relative decrease of the Fe content in the surface (oxy)hydroxide layer of NP-FeCoNiMg-SS-900 electrode before and after aging 1000 h at 1000 mA cm^{-2}. However, the Fe content in bulk of NP-FeCoNiMg-SS-900 hardly have a mass loss before and after aging 1000 h at 1000 mA cm^{-2} (Table S3 and Figure S19), further indicating the composition re-arrangement of surface (oxy)hydroxide layer. After aging 1000 h, the morphology and structure of NP-FeCoNiMg-SS-900 has not a big change compared with the pristine one (Figure S20 and Figure S21), further demonstrating the superior long-term stability. It is obvious that the superior stability of NP-FeCoNiMg-SS-900 electrode is comparable to these electrodes, as shown in the Table S5. These data of the long-term stability for the OER of NP-FeCoNiMg-SS-900 electrode are very impressive and display even higher activity than its initial state after a long period of operation at large current densities, which should be attributed to the outermost metal (oxy)hydroxide layer naturally formed during the OER process. Even if the outermost metal (oxy)hydroxide layer on the electrode surface is peeled off owing to the impact of massive O_2 bubbles generated during the OER process, a new metal (oxy)hydroxide layer can be rapidly formed, ensuring the long-term stability without compromising the electrocatalytic activity. Overall, the long-term stability of NP-

FeCoNiMg-SS-900 electrode compares favorably with RuO_2- and IrO_2-based electrocatalysts in acid medium [62,63] and Ni-based electrocatalysts in alkaline medium [3,32,64–68].

To further provide an insight into the origins of intrinsic activities for the OER, the change of surface structure and characteristics of the sample after aging was confirmed by CV analysis via cycling in 1 M KOH solution with a scan rate of 10 mV s^{-1} between 1.067 and 1.617 V *vs.* RHE (Figure S22). The HRTEM image of the pristine sample (Fig. 5a) exhibits a well-ordered crystalline structure corresponding to γ-Ni based solid solution, including the surface region. However, after cycled by CV scans for 50 times, a metal (oxy)hydroxide layer with a thickness of approximately 9 nm was clearly formed on the outermost surface (Fig. 5b), indicating a surface re-arrangement induced by surface oxidation and atomic/vacancy migration. Combined with the XPS results, it can be concluded that the surface layer should be the metal (oxy)hydroxide layer formed after aging, which is different from the bulk crystal phase. The Raman spectra of NP-FeCoNiMg-SS-900 electrode before and after aging displays an obvious change of surface structure (Figure S23). The strongest peak of the aged sample detected at ~ 532.7 cm^{-1} are best assigned to disordered, doped or alloyed $Ni(OH)_2$ with Fe, Co and Mg, further confirming a metal (oxy)hydroxide layer formed after aging [32,52]. There are some proposed mechanism of dissolution-, dissolution-precipitation or electromigration for the formation of metal (oxy)hydroxide layer during the OER process [47]. Clearly, the metal (oxy)hydroxide layer with a thickness of approximately 9 nm formed on the surface of nanostructured FeCoNi solid solution in Fig. 5 possesses a smooth interface. Hence, the formation of a metal oxyhydroxide layer is more likely the consequence of electromigration via the combination of OH^- and surface ingredients during the initial OER in the alkaline medium.

3. Conclusions

In summary, based on the nanoscale Kirkendall effect, we successfully developed a microwave sintering method to fabricate spongeous FeCoNiMg solid solution with interconnected Kirkendall nanopores and simulated surface compositions of Gibeon meteorites. The as-prepared NP-FeCoNiMg-SS-900 electrodes with a metal (oxy)hydroxide layer of approximately 9 nm thickness formed after aging exhibit superior electrocatalytic activity for the OER possesses in alkaline medium, delivering a low overpotential of 254 mV and a Tafel slope of 37.0 mV dec^{-1}. The high compressive strength (163 MPa) and elastic modulus (2.31 GPa) of NP-FeCoNiMg-SS-900 electrode are satisfactory to ensure the long-term mechanical stability for the OER. The 3D-interconnected nanoporous structure, high conductivity, excellent wettability, proper element compositions, self-renewing surface layer and good mechanical properties of NP-FeCoNiMg-SS-900 electrode brings the superior electrocatalytic activity for the OER in alkaline medium without compromising the long-term stability, which is very competitive among the existing RuO_2-/IrO_2-based and Ni-based electrocatalysts. The studies in this work provide a promising low-cost and environment-friendly approach to prepare nanoporous architectures based on non-precious metal solid solutions by mimicking natural meteorite materials for high-efficiency water electrolysis towards large-scale utilization of clean hydrogen energy.

4. Experimental section

4.1. Materials synthesis.

Commercially-available gas-atomized Fe (12.7 μm, >99.5%), Co (13.7 μm, >99.5%), Ni (17.2 μm, >99.7%) and Mg (75 μm, >99.9%) powders were purchased from Aladdin Chemistry Corp. (Shanghai, China) and employed to fabricate NP-FeCoNiMg-SS electrodes via the microwave-sintering method. The Fe, Co and Ni powders were weighed to have a composition of $Fe_{0.34}Co_{0.11}Ni_{0.55}$ (at.%) according to the metal atom compositions on the surface of the Gibeon meteorites [21]. The spherical Mg powder (10 wt% or 21 at.% of the total mass) were added as the pore-making agent to prepare nanoporous alloys through the nanoscale Kirkendall effect (corrsponding to the No.8 sample in Table S1). A schematic illustration of microwave sintering process for the preparation of NP-FeCoNiMg-SS electrodes is displayed in Figure S24 [41]. For comparison, the control samples with other composition ratios of Fe, Co, Ni and Mg elements were also prepared (Table S1). The powders were homogeneously blended in a planetary ballmill (QM-3SP4, Nanjing University Instrument Plant) at the rotation speed of 250 rpm for 6 h. There are no balls added into the ball-milling tank, avoiding the elemental contamination derived from the friction among powders, balls and tank. The mixed powders were cold-pressed into green compacts (Φ 12 mm × 6 mm) by applied a uniaxial pressure of 580 MPa for 1 min. The green compacts were put in an alumina crucible filled with β-type silicon carbide (β-SiC) particles as microwave susceptors to promote the microwave absorption during the low-temperature heating stage. The alumina crucible was put in a mullite fiber cotton insulation barrel, and the barrel was put in a 2.45 GHz, 5 kW continuously adjustable microwave chamber (NJZ4-3, Nanjing Juequan Corp.). The microwave sintering was carried out under high-purity Ar (>99.999%) atmosphere by microwave heating at a rate of 20–30 °C min^{-1} to 700–1100 °C for 20 min. A Reytek infrared pyrometer was employed test the sample-sintered temperature. For comparison, pure Ni powder and the spherical Mg powders (10 wt% or 21 at.% of the total mass) were mixed to prepare NP-Ni sample via the above method of microwave-sintering at 900 °C for 20 min. The IrO_2 coated Ti substrate (IrO_2/Ti) was fabricated by a thermal decomposition method according

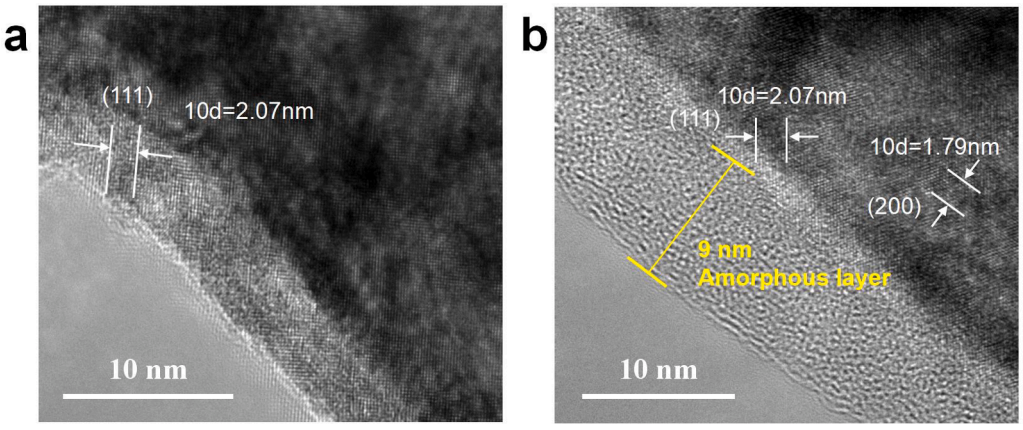

Fig. 5. The formation of (oxy)hydroxide layer after aging. (a) HRTEM image of pristine NP-FeCoNiMg-SS. (b) HRTEM image of NP-FeCoNiMg-SS after CV scans for 50 cycles in 1 M KOH solution with a scan rate of 10 mV s^{-1} between 1.067 and 1.617 V *vs.* RHE.

to a previous report [32].

4.2. Material characterizations

Field emission scanning electron microscopy (FESEM, Zeiss Sigma HD) was employed to observe the morphologies of the samples. The microstructure and compositions of the samples were identified by X-ray diffraction (XRD, Bruker D8 ADVANCE), transmission electron microscopy (TEM, FEI Tecnai G2 F20), energy-dispersive X-ray spectroscopy (EDS, Oxford Instruments), Inductively Coupled Plasma-Optical Emission Spectrometry (ICP-OES, Agilent 730) and X-ray photoelectron spectroscopy (XPS, Axis Ultra DLD, Shimadzu-Kratos). Before the XPS measurement, all the samples were placed into the vacuum drying oven at 60 °C for three day owing to a high water content of nanoporous materials. The tested XPS spectra were calibrated from the binding energy of actual C1S peak to the standard value (284.6 eV). Raman spectra were achieved on a confocal Raman micro-spectroscopy (Thermo Fisher Dxi) with an excitation wavelength of 785 nm. Uniaxial compression tests of cylindrical NP-FeCoNiMg-SS electrodes (Φ 3 mm × 6 mm, L/D = 2.0) were performed on an electronic universal testing machine (WDW-50, Jinan Shijin group Corp.) by the ASTM E9-09 standard test method with a cross-head velocity of 0.2 mm min^{-1} at room temperature. An analytical balance (Mettler Toledo, XS205 Dual Range) with an accuracy 0.01 mg was employed to determine the loading amount of the samples before and after aging.

4.3. Electrochemical measurements

All the OER tests were performed with an electrochemical workstation (CHI-660C, Shanghai CHI Instruments, Inc.) by applying a three-electrode configuration in 1 M KOH solution at 25 °C. The NP-FeCoNiMg-SS electrodes were cut into slices with the thickness of 1 mm. The cell was assembled with a NP-FeCoNiMg-SS electrode (10 mm × 10 mm in area), a saturated calomel electrode (SCE) and a Pt slice electrode serving as the working electrode, reference electrode and counter electrode, respectively. All the tested potentials were calibrated to reversible hydrogen electrode (RHE) [15]. Linear sweep voltammetry (LSV) curves were tested with a scan rate of 1 mV s-1. The *iR*-corrected Tafel slopes were obtained from the LSV curves. The consecutive galvanostatic measurements were performed at different current densities in 1 M KOH solution. Electrochemical impedance spectroscopy (EIS) was performed in a frequency range from 100000 Hz to 0.01 Hz with a 5 mV amplitude at an OER voltage 1.567 mV (*vs* RHE). Long-term stability test of NP-FeCoNiMg-SS-900 electrode for 1000 h at the current density of 1000 mA cm^{-2} was performed with constant-current power supply in 1 M KOH solution. The long-term stability test at the current density of 1000 mA cm^{-2} in 1 M KOH solution was carried out by applying a simple two-electrode water splitting cell assembled with a NP-FeCoNiMg-SS-900 anode and a pure titanium plate (40 mm × 40 mm) cathode. There is a separation distance of approximately 30 mm without a diaphragm between anode and cathode.

The Faradaic efficiency was calculated by using the Eq. (1):

$$\text{Faradaic efficiency} = \frac{\textit{exp}\text{erimental mol of } O_2 \text{ gas}}{\text{theoretical mol of } O_2 \text{ gas}} \times 100\% \quad (1)$$

The theoretical amount of O_2 gas was calculated at corresponding time intervals from Faraday's law, Eq. (2):

$$m = \frac{i \times t}{z \times F} \quad (2)$$

where m is the number of mol, i is the current (ampere), t is the time (second), z *represents* the transfer of electrons (for OER $z = 4$), and F denotes as the Faraday constant (96,485 C mol^{-1}).

Declaration of Competing Interest

The authors declare that they have no known competing financial interests or personal relationships that could have appeared to influence the work reported in this paper.

Acknowledgment

Funding: This work was supported by the National Key R&D Program of China (2017YFA0208200 and 2016YFB0700600), the National Natural Science Foundation of China (51862026, 51562027, 51101085, 21872069, 21573108 and 51761135104), the Aeronautical Science Foundation of China (2017ZF56027), the Natural Science Foundation of Jiangxi Province (20192ACBL21048), the Natural Science Foundation of Jiangsu Province (BK20180008), the Fundamental Research Funds for the Central Universities, and the Excellent Youth Foundation of Jiangxi Scientific Committee (20171BCB23054).

Author contributions

Z.G. Ye and J.L. Xu conceived the idea of this study and designed the experiments. B.Y. Hao and L.L. Li performed the sample synthesis. B.Y. Hao performed the material characterizations and electrochemical measurements. Z.G. Yu, J.L. Xu, G. Ma, J.T. Huang, X.Y. Peng, D.S. Li and Z. Jin analyzed the data and discussed the results. Z.G. Ye and Z. Jin co-wrote and revised the manuscript. Z. Jin supervised the project.

Appendix A. Supplementary data

Supplementary data to this article can be found online at https://doi.org/10.1016/j.cej.2020.128340.

References

[1] S. Anantharaj, S.R. Ede, K. Sakthikumar, K. Karthick, S. Mishra, S. Kundu, Recent trends and perspectives in electrochemical water splitting with an emphasis on sulfide, selenide, and phosphide catalysts of Fe, Co, and Ni: a review, ACS Catal. 6 (2016) 8069–8097.
[2] Z.H. Hua, J.T. Huang, Y. Luo, M.Q. Liu, X.B. Li, M.G. Yan, Z.G. Ye, Z. Chen, Z. J. Feng, S.F. Huang, Wrinkled Ni-doped Mo_2C coating on carbon fiber paper: an advanced electrocatalyst prepared by molten-salt method for hydrogen evolution reaction, Electrochim. Acta 319 (2019) 293–301.
[3] X.Y. Lu, C. Zhao, Electrodeposition of hierarchically structured three-dimensional nickel-iron electrodes for efficient oxygen evolution at high current densities, Nat. Commun. 6 (2015) 6616.
[4] S. Trasatti, Electrodes of Conductive Metallic Oxides, Part A, Elsevier, 1980.
[5] H.X. Liu, Y.R. Wang, X.Y. Lu, Y. Hu, G.Y. Zhu, R.P. Chen, L.B. Ma, H.F. Zhu, Z. X. Tie, J. Liu, Z. Jin, The effects of Al substitution and partial dissolution on ultrathin NiFeAl trinary layered double hydroxide nanosheets for oxygen evolution reaction in alkaline solution, Nano Energy 35 (2017) 350–357.
[6] Y. Yang, H.L. Fei, G.D. Ruan, C.S. Xiang, J.M. Tour, Efficient electrocatalytic oxygen evolution on amorphous nickel-cobalt binary oxide nanoporous layers, ACS Nano 8 (2014) 9518–9523.
[7] H. Liang, F. Meng, M. Cabán-Acevedo, L. Li, A. Forticaux, L. Xiu, Z. Wang, S. Jin, Hydrothermal continuous flow synthesis and exfoliation of NiCo layered double hydroxide nanosheets for enhanced oxygen evolution catalysis, Nano Lett. 15 (2015) 1421–1427.
[8] Z. Ye, C. Qin, G. Ma, X. Peng, T. Li, D. Li, Z. Jin, Cobalt-iron oxide nanoarrays supported on carbon fiber paper with high stability for electrochemical oxygen evolution at large current densities, ACS Appl. Mater. Interfaces 10 (2018) 39809–39818.
[9] Y.H. Dou, T. Liao, Z.Q. Ma, D.L. Tian, Q.N. Liu, F. Xiao, Z.Q. Sun, J.H. Kim, S. X. Dou, Graphene-like holey Co3O4 nanosheets as a highly efficient catalyst for oxygen evolution reaction, Nano Energy 30 (2016) 267–275.
[10] H. Osgood, S.V. Devaguptapu, H. Xu, J. Cho, G. Wu, Transition metal (Fe Co, Ni, and Mn) oxides for oxygen reduction and evolution bifunctional catalysts in alkaline media, Nano Today 11 (2016) 601–625.
[11] J. Han, S. Dong, E. Wang, Transition-metal (Co, Ni, and Fe)-based electrocatalysts for the water oxidation reaction, Adv. Mater. 28 (2016) 9266–9291.
[12] X. Liu, W. Liu, M. Ko, M. Park, M.G. Kim, P. Oh, S. Chae, S. Park, A. Casimir, G. Wu, J. Cho, Metal (Ni, Co)-metal oxides/graphene nanocomposites as multifunctional electrocatalysts, Adv. Funct. Mater. 25 (2015) 5799–5808.
[13] A. Kargar, S.J. Kim, P. Allameh, C. Choi, N. Park, H. Jeong, Y. Pak, G.Y. Jung, X. Q. Pan, D.L. Wang, S. Jin, p-Si/SnO2/Fe2O3 core/shell/shell nanowire photocathodes for neutral pH water splitting, Adv. Funct. Mater. 25 (2015) 2609–2615.

[14] Y.T. Meng, W.Q. Song, H. Huang, Z. Ren, S.Y. Chen, S.L. Suib, Structure-property relationship of bifunctional MnO_2 nanostructures: highly efficient, ultra-stable electrochemical water oxidation and oxygen reduction reaction catalysts identified in alkaline media, J. Am. Chem. Soc. 136 (2014) 11452–11464.

[15] Z.G. Ye, T. Li, G. Ma, Y.H. Dong, X.L. Zhou, Metal-Ion (Fe, V Co, and Ni)-doped MnO2 ultrathin nanosheets supported on carbon fiber paper for the oxygen evolution reaction, Adv. Funct. Mater. 27 (2017) 1704083.

[16] G. Gupta, K. Selvakumar, M. Mamlouk, N. Lakshminarasimhan, S.M. Senthil Kumar, The effects of morphology, microstructure and mixed-valent states of MnO_2 on the oxygen evolution reaction activity in alkaline anion exchange membrane water electrolysis, J. Power Sources 461 (2020), 228131.

[17] Y. Li, L. Zhang, J. Peng, W. Zhang, K. Peng, Magnetic field enhancing electrocatalysis of Co_3O_4/NF for oxygen evolution reaction, J. Power Sources 433 (2019), 226704.

[18] C. Li, B. Zhang, Y. Li, S. Hao, X. Cao, G. Yang, J. Wu, Y. Huang, Self-assembled Cu-Ni bimetal oxide 3D in-plane epitaxial structures for highly efficient oxygen evolution reaction, Appl. Catal. B-Environ. 244 (2019) 56–62.

[19] D. Tang, R. Zhao, C. Shen, Y. Han, X. Wu, H. Wu, G. Diao, M. Chen, High electrocatalytic performance of bimetallic sulfides dodecahedral nanocages $(Co_xM_{1-x})_9S_8$/M/N–C (M=Ni, Cu) for triiodide reduction reaction and oxygen evolution reaction, Electrochim. Acta 324 (2019), 134888.

[20] J.F. Qin, M. Yang, T.S. Chen, B. Dong, S. Hou, X. Ma, Y.N. Zhou, X.L. Yang, J. Nan, Y.M. Chai, Ternary metal sulfides MoCoNiS derived from metal organic frameworks for efficient oxygen evolution, Int. J. Hydrogen Energy 45 (2020) 2745–2753.

[21] H.H. Zhao, Y. Yang, X.P. Dai, H.Y. Qiao, J.X. Yong, X.B. Luan, L. Yu, C.L. Luan, Y. Wang, X. Zhang, NiCo-DH nanodots anchored on amorphous NiCo-sulfide sheets as efficient electrocatalysts for oxygen evolution reaction, Electrochim. Acta 295 (2019) 1085–1092.

[22] L.Z. Zhuang, L. Ge, Y.S. Yang, M.R. Li, Y. Jia, X.D. Yao, Z.H. Zhu, Ultrathin iron-cobalt oxide nanosheets with abundant oxygen vacancies for the oxygen evolution reaction, Adv. Mater. 29 (2017) 1606793.

[23] L. Xu, Q.Q. Jiang, Z.H. Xiao, X.Y. Li, J. Huo, S.Y. Wang, L.M. Dai, Plasma-engraved Co3O4 nanosheets with oxygen vacancies and high surface area for the oxygen evolution reaction, Angew. Chem. 128 (2016) 5363–5367.

[24] C.Z. Yuan, L. Yang, L.R. Hou, L.F. Shen, X.G. Zhang, X.W. Lou, Growth of ultrathin mesoporous Co3O4 nanosheet arrays on Ni foam for high-performance electrochemical capacitors, Energy Environ. Sci. 5 (2012) 7883–7887.

[25] M. Chauhan, K.P. Reddy, C. Gopinath, S. Deka, Copper cobalt sulfide nanosheets realizing a promising electrocatalytic oxygen evolution reaction, ACS Catal. 7 (2017) 5871–5879.

[26] X. Xu, F. Song, X. Hu, A nickel iron diselenide-derived efficient oxygen-evolution catalyst, Nat. Commun. 7 (2016) 12324.

[27] Z. Liu, B. Tang, X.C. Gu, H. Liu, L.G. Feng, Selective structure transformation for $NiFe/NiFe_2O_4$ embedded porous nitrogen-doped carbon nanosphere with improved oxygen evolution reaction activity, Chem. Eng. J. 395 (2020), 125170.

[28] H. Liu, Z. Liu, F.L. Wang, L.G. Feng, Efficient catalysis of N doped NiS/NiS_2 heterogeneous structure, Chem. Eng. J. 397 (2020), 125507.

[29] X.C. Gu, Z. Liu, H. Liu, C.G. Pei, L.G. Feng, Fluorination of ZIF-67 framework templated Prussian blue analogue nano-box for efficient electrochemical oxygen evolution reaction, Chem. Eng. J. 403 (2020), 126371.

[30] H. Liu, M. Zha, Z. Liu, J.Q. Tian, G.Z. Hu, L.G. Feng, Synergistically boosting oxygen evolution reaction of Fe-MOF by Ni doping and fluorination, Chem. Commun. 56 (57) (2020).

[31] B. Tang, X.D. Yang, Z.H. Kang, L.Z. Feng, Crystallized $RuTe_2$ as unexpected bifunctional catalyst for overall water splitting, Appl. Catal. B 278 (2020), 119281.

[32] F.L. Formal, N. Guijarro, W.S. Bourée, A. Gopakumar, M.S. Prévot, A. Daubry, L. Lombardo, C. Sornay, J. Voit, A. Magrez, P.J. Dyson, K. Sivula, A Gibeon meteorite yields a high-performance water oxidation electrocatalyst, Energy Environ. Sci. 9 (2016) 3448–3455.

[33] T. He, W. Wang, X. Yang, Z. Cao, Q. Kuang, Z. Wang, Z. Shan, M. Jin, Y. Yin, Inflating hollow nanocrystals through a repeated Kirkendall cavitation process, Nat. Commun. 8 (2017) 1261.

[34] Y. Yin, R.M. Rioux, C.K. Erdonmez, S. Hughes, G.A. Somorjai, A.P. Alivisatos, Formation of hollow nanocrystals through the nanoscale Kirkendall Effect, Science 304 (2004) 711–714.

[35] H.J. Fan, M. Knez, R. Scholz, K. Nielsch, E. Pippel, D. Hesse, M. Zacharias, U. Gosele, Monocrystalline spinel nanotube fabrication based on the Kirkendall Effect, Nat. Mater. 5 (2006) 627–631.

[36] E. González, J. Arbiol, V.F. Puntes, Carving at the nanoscale: sequential galvanic exchange and Kirkendall growth at room temperature, Science 334 (2011) 1377–1380.

[37] J.X. Wang, C. Ma, Y.M. Choi, D. Su, Y.M. Zhu, P. Liu, R. Si, M.B. Vukmirovic, Y. Zhang, R.R. Adzic, Kirkendall effect and lattice contraction in nanocatalysts: a new strategy to enhance sustainable activity, J. Am. Chem. Soc. 133 (2011) 13551–13557.

[38] Y. Yin, C.K. Erdonmez, A. Cabot, S. Hughes, A.P. Alivisatos, Colloidal synthesis of hollow cobalt sulfide nanocrystals, Adv. Funct. Mater. 16 (2006) 1389–1399.

[39] X. Liang, X. Wang, Y. Zhuang, B. Xu, S.M. Kuang, Y.D. Li, Formation of CeO2-ZrO2 solid solution nanocages with controllable structures via Kirkendall effect, J. Am. Chem. Soc. 130 (2008) 2736–2737.

[40] A.D. Smigelskas, E.O. Kirkendall, Zinc diffusion in alpha-brass, Trans. Am. Inst. Mining Metall. Eng. 171 (1947) 130–142.

[41] J. Xu, S. Tao, L. Bao, J. Luo, Y. Zheng, Effects of Mo contents on the microstructure, properties and cytocompatibility of the microwave sintered porous Ti-Mo alloys, Mat. Sci. Eng. C-Mater. 97 (2019) 156–165.

[42] M. Oghbaei, O. Mirzaee, Microwave versus conventional sintering: a review of fundamentals, advantages and applications, J. Alloy Compd. 494 (2010) 175–189.

[43] Y.V. Bykov, S.V. Egorov, A.G. Eremeev, V.V. Kholoptsev, I.V. Plotnikov, K. I. Rybakov, A.A. Sorokin, S.S. Balabanov, A.V. Belyaev, Ultra-rapid Microwave Sintering of Pure and Y_2O_3-doped $MgAl_2O_4$, J. Am. Chem. Soc. 102 (2019) 559–568.

[44] P. Villars, L.D. Calvert, Pearson's Handbook of Crystallographic Data for Intermetallic Phases, 2nd Edition, ASM, Metals Park, Ohio, 1991.

[45] A. Grimaud, A. Demortière, M. Saubanère, W. Dachraoui, M. Duchamp, M. L. Doublet, J.M. Tarascon, Activation of surface oxygen sites on an iridium-based model catalyst for the oxygen evolution reaction, Nat. Energy 2 (2016) 16189.

[46] A.P. Grosvenor, B.A. Kobe, M.C. Biesinger, N.S. McIntyre, Investigation of multiplet splitting of Fe 2p XPS spectra and bonding in iron compounds, Surf. Interface Anal. 36 (2004) 1564–1574.

[47] H. Schafer, S. Sadaf, L. Walder, K. Kuepper, S. Dinklage, J. Wollschlager, L. Schneider, M. Steinhart, J. Hardege, D. Daum, Stainless steel made to rust: a robust water-splitting catalyst with benchmark characteristics, Energy Environ. Sci. 8 (2015) 2685–2697.

[48] M.C. Biesinger, B.P. Payne, A.P. Grosvenor, L.W.M. Lau, A.R. Gerson, R.S.C. Smart, Resolving surface chemical states in XPS analysis of first row transition metals, oxides and hydroxides: Cr, Mn, Fe, Co and Ni, Appl. Surf. Sci. 257 (2011) 2717–2730.

[49] J.F. Moulder, J. Chastain (eds.) in Handbook of X-ray Photoelectron Spectroscopy: a Reference Book of Standard Spectra for Identification and Interpretation of XPS Data, Perkin-Elmer Corporation 1992 Minn, update Eden Prairie.

[50] H.B. Li, M.H. Yu, F.X. Wang, P. Liu, Y. Liang, J. Xiao, C.X. Wang, Y.X. Tong, G. W. Yang, Amorphous nickel hydroxide nanospheres with ultrahigh capacitance and energy density as electrochemical pseudocapacitor materials, Nat. Commun. 4 (2013) 1894.

[51] D.E. Haycock, M. Kasrai, C.J. Nicholls, D.S. Urch, The electronic structure of magnesium hydroxide (brucite) using X-ray emission, X-ray photoelectron, and auger spectroscopy, J. Chem. Soc., Dalton Trans. (12) (1978) 1791, https://doi.org/10.1039/dt9780001791.

[52] M.W. Louie, A.T. Bell, An investigation of thin-film Ni-Fe oxide catalysts for the electrochemical evolution of oxygen, J. Am. Chem. Soc. 135 (2013) 12329–12337.

[53] A. Bergmann, E. Martinez-Moreno, D. Teschner, P. Chernev, M. Gliech, J. Ferreira de Araújo, T. Reier, H. Dau, P. Strasser, Reversible amorphization and the catalytically active state of crystalline Co_3O_4 during oxygen evolution, Nat. Commun. 6 (2015) 8625.

[54] F. Dionigi, Z.H. Zeng, I. Sinev, T. Merzdorf, S. Deshpande, N.B. Lopez, S. Kunze, I. Zegkinoglou, H. Sarodnik, D. Fan, A. Bergmann, J. Drnec, D.F. Araujo, M. Gliech, D. Teschner, J. Zhu, W.X. Li, J. Greeley, B.R. Cuenya, P. Strasser, In-situ structure and catalytic mechanism of NiFe and CoFe layered double hydroxides during oxygen evolution, Nat. Commun. 11 (2020) 2522.

[55] D. Friebel, M.W. Louie, M. Bajdich, K.E. Sanwald, Y. Cai, A.M. Wise, M.J. Cheng, D. Sokaras, T.C. Weng, R. Alonso-Mori, R.C. Davis, J.R. Bargar, J.K. Norskov, A. Nilsson, A.T. Bell, Identification of highly active Fe sites in (Ni, Fe)OOH for electrocatalytic water splitting, J. Am. Chem. Soc. 137 (2015) 1305–1313.

[56] X.L. Zhu, C. Tang, H.F. Wang, B.Q. Li, Q. Zhang, C.Y. Li, C.H. Yang, F. Wei, Monolithic-structured ternary hydroxides as freestanding bifunctional electrocatalysts for overall water splitting, J. Mater. Chem. A 4 (2016) 7245–7250.

[57] C.Q. Dong, L.L. Han, C. Zhang, Z.H. Zhang, Scalable dealloying route to mesoporous ternary CoNiFe layered double hydroxides for efficient oxygen evolution, ACS Sustainable Chem. Eng. 6 (2018) 16096–16104.

[58] Z.C. Wu, X. Wang, J.S. Huang, F. Gao, A Co-doped Ni-Fe mixed oxide mesoporous nanosheet array with low overpotential and high stability towards overall water splitting, J. Mater. Chem. A 6 (2018) 167–178.

[59] A.C. Thenuwara, N.H. Attanayake, J. Yu, J.P. Perdew, E.J. Elzinga, Q.M. Yan, D. R. Strongin, Cobalt intercalated layered NiFe double hydroxides for the oxygen evolution reaction, J. Phys. Chem. B 122 (2018) 847–854.

[60] M.B. Stevens, L.J. Enman, E.H. Korkus, J. Zaffran, C.D.M. Trang, J. Asbury, M. J. Kast, M.C. Toroker, S.E. Boettcher, Ternary Ni-Co-Fe oxyhydroxide oxygen evolution catalysts: intrinsic activity trends, electrical conductivity, and electronic band structure, Nano Res. 12 (2019) 2288–2295.

[61] C. Wei, S.N. Sun, D. Mandler, X. Wang, S.Z. Qiao, Z.C. Xu, Approaches for measuring the surface areas of metal oxide electrocatalysts for determining their intrinsic electrocatalytic activity, Chem. Soc. Rev. 48 (2019) 2518–2534.

[62] Y. Lee, J. Suntivich, K.J. May, E.E. Perry, Y. Shao-Horn, Synthesis and activities of rutile IrO_2 and RuO_2 nanoparticles for oxygen evolution in acid and alkaline solutions, J. Phys. Chem. Lett. 3 (2012) 399–404.

[63] J. Hu, H. Meng, J. Zhang, C. Cao, Degradation mechanism of long service life Ti/IrO_2-Ta_2O_5 oxide anodes in sulphuric acid, Corros. Sci. 44 (2002) 1655–1668.

[64] M.W. Louie, A.T. Bell, An advanced Ni-Fe layered double hydroxide electrocatalyst for water oxidation, J. Am. Chem. Soc. 135 (2013) 8452–8455.

[65] W.J. Zhou, X.J. Wu, X.H. Cao, X. Huang, C.L. Tan, J. Tian, H. Liu, J.Y. Wang, H. Zhang, Ni_3S_2 nanorods/Ni foam composite electrode with low overpotential for electrocatalytic oxygen evolution, Energy Environ. Sci. 6 (2013) 2921.

[66] L. Trotochaud, S.L. Young, J.K. Ranney, S.W. Boettcher, Nickel-iron oxyhydroxide oxygen-evolution electrocatalysts: the role of intentional and incidental iron incorporation, J. Am. Chem. Soc. 136 (2014) 6744–6753.

[67] K. Fominykh, P. Chernev, I. Zaharieva, J. Sicklinger, G. Stefanic, M. Doblinger, A. Muller, A. Pokharel, S. Bocklein, C. Scheu, T. Bein, D. Fattakhova-Rohlfing, Iron-doped nickel oxide nanocrystals as highly efficient electrocatalysts for alkaline water splitting, ACS Nano 9 (2015) 5180–5188.

[68] Y.F. Zhao, X.D. Jia, G.B. Chen, L. Shang, G.I.N. Waterhouse, L.Z. Wu, C.H. Tung, D. O'Hare, T.R. Zhang, Ultrafine NiO nanosheets stabilized by TiO_2 from

monolayer NiTi-LDH precursors: an active water oxidation electrocatalyst, J. Am. Chem. Soc. 138 (2016) 6517–6524.